

Hydrodynamics substantially affects induced structure formation in magnetic fluids

Henning Reinken,^{1,*} Markus Heiber,¹ Takeaki Araki,² and Andreas M. Menzel^{1,†}

¹*Institut für Physik, Otto-von-Guericke-Universität Magdeburg, Universitätsplatz 2, 39106 Magdeburg, Germany*

²*Department of Physics, Kyoto University, Kyoto 606-8502, Japan*

(Dated: February 5, 2026)

Magnetorheological fluids consist of micrometer-sized magnetic particles in a carrier liquid. Sufficiently strong external magnetic fields lead to the formation of string-like particle aggregates. We demonstrate that hydrodynamic interactions, that is, mutual couplings via induced flows, play a substantial role during structure formation. Hydrodynamics supports the emergence of string-like aggregates, while magnetic interactions align them. This fundamental insight is substantial from an application perspective, due to the enormous technical importance and potential of magnetorheological fluids.

For decades, the appealing properties of magnetic fluids have been explored. Stabilizing nanometer-sized magnetic particles in carrier liquids leads to magnetic suspensions. Such ferrofluids [1] are of outstanding technical relevance, considering, for instance, their use in hard drives or loudspeaker components. Suspensions of larger, micrometer-sized magnetic or magnetizable particles are referred to as magnetorheological fluids [2, 3]. The name reflects their remarkable feature of tunable shear viscosity. More precisely, the magnitude of the overall viscosity can be substantially affected by application of a sufficiently strong, homogeneous, external magnetic field [2, 3].

The background of this so-called magnetoviscous effect had been discussed for a longer while. Its root was searched for in rotational blocking of individual particles by external magnetic fields [4]. Yet, this effect is often not sufficient to explain the observed substantial change in overall viscosity in magnetorheological fluids. Instead, the magnetically induced formation of string-like aggregates plays a central role in revealing the source of the magnetoviscous effect [3, 5]. When the formation of string-like aggregates is magnetically induced and simultaneously their rotation is magnetically hindered, overall shear resistance is significantly affected. The phenomenon is based on collective processes of microscopic, particulate structure formation.

There are further circumstances where the formation of string-like aggregates of magnetic particles becomes important. For instance, magnetorheological elastomers consist of micrometer-sized magnetic particles fixated in an elastic carrier medium [6–9]. These materials likewise show a magnetorheological effect. Imposed, homogeneous, external magnetic fields affect their overall stiffness and damping behavior [10–13]. Moreover, they change their shape in external magnetic fields. This magnetostrictive behavior [14–19] suggests their use as soft actuators, soft robots, or magnetic valves [20–22]. It turns out that internal structuring of the magnetic particle distribution significantly affects these types of behavior. String-like aggregates can substantially enhance the nature and magnitudes of both magnetorheological and

magnetostrictive effects [6, 15, 17, 23–30].

In reality, particulate strings are introduced in the still fluid polymeric suspension by exposure to strong, homogeneous, external magnetic fields [3, 5, 31]. These structures are locked in when establishing the permanent elastic carrier medium by chemically crosslinking the surrounding polymeric suspension. Thus, similarly, during this process magnetically induced structure formation in fluid systems plays a substantial role. There are various other contexts in which string-like aggregates of magnetic particles are formed. One example are living biological microorganisms that use strings of magnetic particles for orientation in the Earth’s magnetic field [32].

Overall, we may conclude that formation of string-like aggregates from microscopic magnetic particles in surrounding fluids is central in nature and in technology. It is therefore surprising that the role of the carrier liquid during this structural formation process has hardly been considered. Exceptions are given by evaluations of structure factors for particle distributions in magnetic liquids [33]. Yet, an explicit account for the role of fluid flows induced by the magnetically driven particles is missing in the context of magnetically induced structure formation. This is even more surprising when we recall that hydrodynamic interactions promote the formation of string-like structures already for nondirectional, isotropic interactions between mutually attracting particles [34–36]. Thus, we expect that hydrodynamics supports the formation of string-like particulate structures also in magnetic fluids, where the driving force induced by an external magnetic field leads to anisotropic particle interactions.

We here address this point. The formation of string-like aggregates of magnetic particles in a fluid suspension is compared between the cases of including or excluding hydrodynamic couplings. In this way, we demonstrate that hydrodynamic interactions play an important role in structure formation in magnetic suspensions. They significantly support structuring, while the magnetic field imposes an overall direction of anisotropy that aligns the resulting aggregates.

Corresponding descriptions pose a challenge. First,

couplings between discrete particles and continuous surrounding carrier media represent a significant task. Correct boundary conditions on the moving surfaces of the particles must be maintained. We here assume no-slip surface conditions. Second, the magnetic particles approach each other from the distance until they are basically in contact. Thus, far-field hydrodynamic expansions [37] are not sufficient, and finite-element methods face the problem of strongly distorted calculation meshes [38]. Moreover, the system must be tracked for sufficiently long time scales. Additionally, magnetic interactions must be included in a consistent manner.

To face these challenges, we build on a method that considers the particles as parts of the fluid, yet, with significantly enhanced viscosity that hinders their deformation [34, 36, 39–42]. Thus, couplings between particles and fluid as well as hydrodynamic interactions are intrinsic to the method. Approach into virtual contact is supported. We extend this “fluid particle dynamics” (FPD) method [34, 36, 43] by the influence of externally imposed magnetic fields on magnetizable particles. Comparison with “dry” systems in the absence of enclosing fluids reveals the importance of fluid flows on magnetically induced structure formation.

Key to the FPD method [34, 36, 43] is to represent the presence of any particle i through a continuous field ϕ_i . Similarly to phase-field models [44, 45], this field distinguishes between the inside and the outside of the particle, with $\phi_i = 1$ inside, $\phi_i = 0$ outside, and a smooth transition in between. We set ϕ_i as

$$\phi_i(\mathbf{r}) = [\tanh\{(a - |\mathbf{r} - \mathbf{R}_i|)/c\} + 1]/2, \quad (1)$$

where \mathbf{R}_i is the particle position, a its radius, and c the thickness of the interface region between particle and fluid. The particles are considered identical and as part of the fluid, albeit with significantly increased viscosity η_p compared to the fluid viscosity η_s . We define their ratio R via $\eta_p = R\eta_s$. Summing over all particles, we obtain the total phase field ϕ_{tot} as

$$\phi_{\text{tot}}(\mathbf{r}) = \sum_{i=1}^N \phi_i(\mathbf{r}), \quad (2)$$

where N is the total number of particles. As a function of space, the viscosity follows as

$$\eta(\mathbf{r}) = \eta_s + (R - 1)\eta_s\phi_{\text{tot}}(\mathbf{r}). \quad (3)$$

The viscosity field enters the Navier–Stokes equation

$$\rho\partial_t\mathbf{v} + \rho\mathbf{v} \cdot \nabla\mathbf{v} = \mathbf{f} - \nabla p + \nabla \cdot [\eta\{(\nabla\mathbf{v}) + (\nabla\mathbf{v})^\top\}], \quad (4)$$

which governs the dynamics of the velocity field \mathbf{v} . Here, we assume that the mass density of the particles is equal to that of the fluid. Moreover, we restrict ourselves to incompressible fluids, that is, $\nabla \cdot \mathbf{v} = 0$.

The Navier–Stokes equation (4) further includes a force density field \mathbf{f} , which is determined from the forces \mathbf{F}_i acting on the particles via

$$\mathbf{f}(\mathbf{r}) = \frac{1}{V_p} \sum_{i=1}^N \mathbf{F}_i\phi_i(\mathbf{r}). \quad (5)$$

V_p is the particle volume in three dimensions or area in two dimensions. The force acting on each particle, thus transmitted to the fluid, is equally distributed over the nondeformable particle body. We distinguish between forces stemming from a pair potential, characterizing, for example, steric effects, and magnetic forces between particles. For the former, we here use the conventional Lennard–Jones potential [34], which as a function of the center-to-center distance r between two particles reads

$$V(r) = \epsilon \left[\left(\frac{\sigma}{r}\right)^{12} - \left(\frac{\sigma}{r}\right)^6 \right]. \quad (6)$$

ϵ is the interaction strength and $\sigma = 2a$ the interaction range.

We extend the method to include magnetic forces between the particles. Often, these are described via dipole–dipole interactions based on the far-field contributions to the induced magnetic fields. However, during structure formation, particles approach until virtually in contact. Thus, more refined methods are required, which accurately describe magnetic effects even for small distances between particles. Therefore we spatially resolve magnetization within the particles. Utilizing the phase fields ϕ_i , the magnetization field \mathbf{M} is determined from the local magnetic field \mathbf{H} using the Langevin function

$$\mathbf{M} = M_{\text{sat}} \left[\coth(\alpha\phi_{\text{tot}}|\mathbf{H}|) - \frac{1}{\alpha\phi_{\text{tot}}|\mathbf{H}|} \right] \frac{\mathbf{H}}{|\mathbf{H}|}. \quad (7)$$

The parameter α determines the linearized relation between \mathbf{M} and \mathbf{H} , while M_{sat} is the saturation value of the magnetization [46]. The magnetic field \mathbf{H} , in turn, is composed of an applied uniform external magnetic field \mathbf{H}_{ext} and the field induced by the magnetized particles themselves. To determine this additional contribution, we solve Maxwell’s equations in space, that is,

$$\nabla \cdot \mathbf{B} = 0, \quad \nabla \times \mathbf{H} = \mathbf{0}, \quad (8)$$

where \mathbf{B} and \mathbf{H} are related via

$$\mathbf{B} = \mu_0(\mathbf{M} + \mathbf{H}). \quad (9)$$

Having obtained \mathbf{M} and \mathbf{B} , the magnetic force density can be calculated via $\mathbf{f}^{\text{mag}} = \mathbf{M} \cdot \nabla\mathbf{B}$ [15, 47–49]. The magnetic forces acting on the particles are obtained as

$$\mathbf{F}_i^{\text{mag}} = \int d\mathbf{r} \mathbf{M}_i \cdot \nabla\mathbf{B}. \quad (10)$$

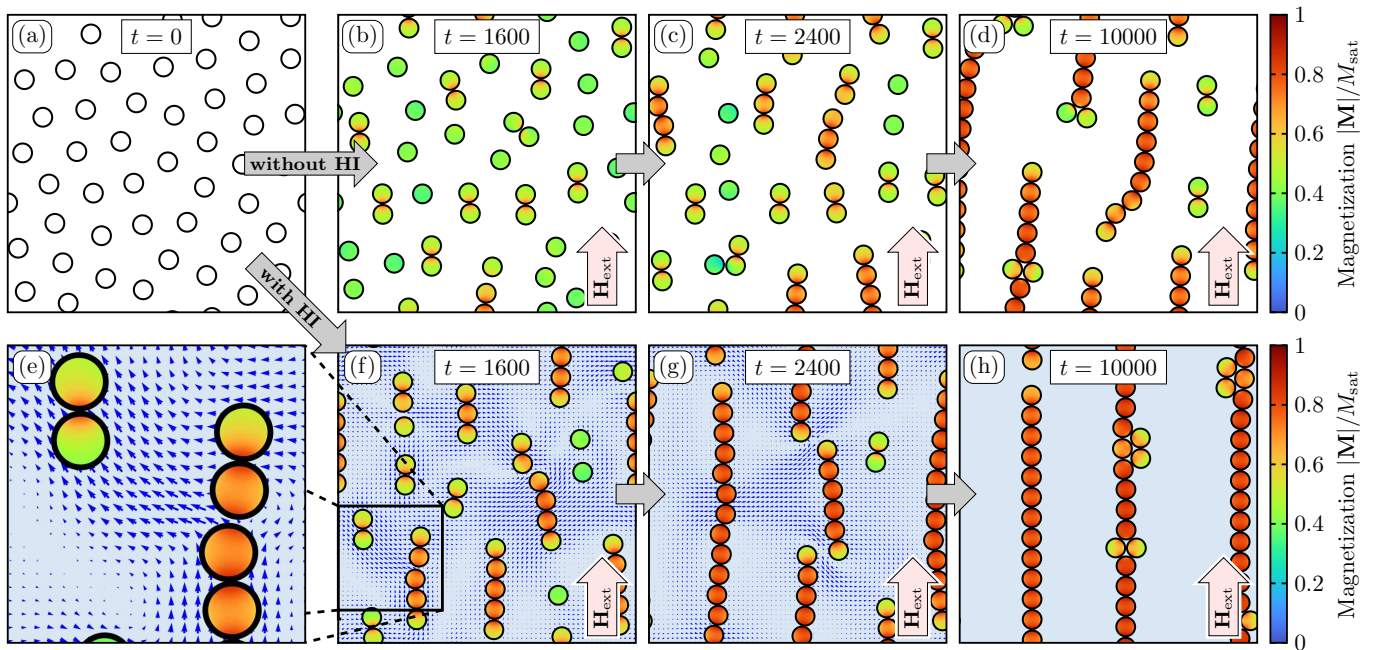


FIG. 1. Structure formation with and without hydrodynamic interactions (HI) for an area fraction of $\theta \approx 0.15$. (a) Simulations start from the same configuration of roughly equally distributed particles. (b–d) Snapshots of the “dry” system at times $t = 1600$, 2400 , and 10000 . The color scale refers to the magnetization field within the particles. (f–h) Snapshots of the system involving hydrodynamic interactions and fluid flows at the same times. Blue arrows indicate the flow field. (e) Magnified part of (f) showing the emergence of large-scale flows and the mutual amplification of local magnetization for particles that are close to each other. The external field strength is set to $|\mathbf{H}_{\text{ext}}|/M_{\text{sat}} = 0.2$.

\mathbf{M}_i is the magnetization field within particle i , calculated in analogy to Eq. (7), but using the phase field ϕ_i instead of ϕ_{tot} .

To determine the actual motion of the particles, we return to the discrete particle level. The particle velocities \mathbf{V}_i are obtained as averages of the velocity field \mathbf{v} over the particle bodies,

$$\mathbf{V}_i = \frac{1}{V_p} \int d\mathbf{r} \mathbf{v}(\mathbf{r}) \phi_i(\mathbf{r}). \quad (11)$$

Time integration of \mathbf{V}_i updates the particle positions.

In practice, the different steps of the FPD method are performed in sequence. We first calculate the forces acting on the particles, including the magnetic forces as described above. These enter the calculations of the flow field, which is performed using an implicit Euler approach combined with a pseudospectral method [50]. Particle positions are then updated according to Eq. (11). Afterwards, the sequence repeats. We refer to the Supplemental Material for further details [51].

To evaluate the equations numerically, we rescale our quantities. We use the particle radius a as a length scale and introduce the time scale $\sqrt{\rho a^5/\epsilon}$, which involves the strength of the Lennard–Jones potential. The strength of viscous forces is determined by $C_{\text{visc}} = \eta_s \sqrt{a}/(\rho \epsilon)$, which we set $C_{\text{visc}} = 1$. This leads to observed local Reynolds numbers $\text{Re} \approx 10^{-2}$. Thus, inertial effects are

not expected to play a significant role. The strength of magnetic forces is characterized by $C_{\text{mag}} = \mu_0 M_{\text{sat}}^2 a^3/\epsilon$. We set $C_{\text{mag}} = 1$ so that the strength of Lennard–Jones and magnetic forces are comparable. The magnetic parameters are set to $M_{\text{sat}} = 3.333 \times 10^5 \text{ A m}^{-1}$ and $\alpha = 1.179 \times 10^{-4} \text{ m A}^{-1}$, corresponding to paramagnetic nickel particles [46]. More details on rescaling are found in the Supplemental Material [51].

Predominantly, we aim to identify and illustrate the impact of hydrodynamics on the two-dimensional structure formation. To this end, we compare the simulations that include hydrodynamic effects described by the Navier–Stokes equation (4) to discrete particle dynamics in the absence of fluid interactions. In the latter “dry” case, particle velocities \mathbf{V}_i are not determined from the flow field, but directly from Newton’s second law with an effective linear friction parameter γ ,

$$\frac{d\mathbf{V}_i}{dt} = \mathbf{F}_i^{\text{mag}} + \mathbf{F}_i^{\text{LJ}} - \gamma \mathbf{V}_i, \quad (12)$$

in rescaled units. \mathbf{F}_i^{LJ} are the forces due the Lennard–Jones potential. We set $\gamma = 50$, which results in an aggregation time scale comparable to structure formation under hydrodynamic couplings.

We start our numerical simulations from initial configurations of roughly equally spaced particles, see Fig. 1(a) for a snapshot. Once the magnetic field is turned on, the

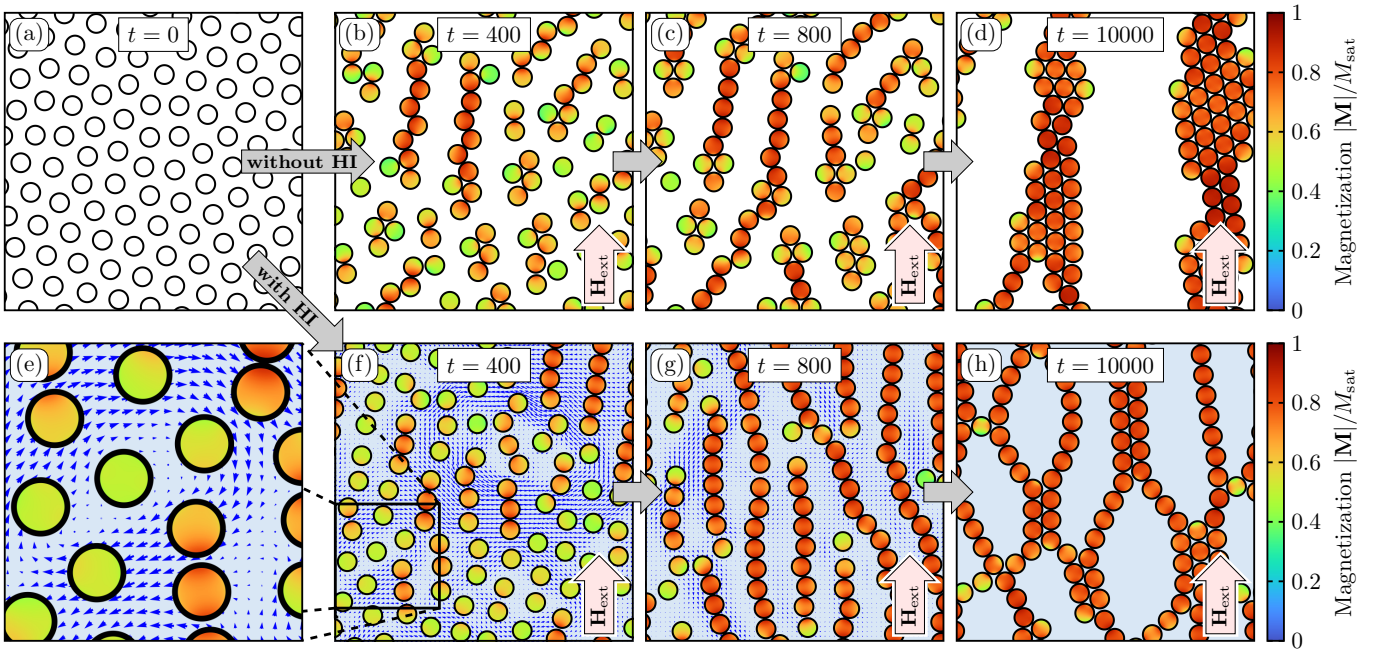


FIG. 2. Same as in Fig. 1, yet for an elevated area fraction of $\theta \approx 0.31$ and snapshots in (b–d) and (f–h) taken at times $t = 400, 800,$ and 10000 . Here, chain formation promoted by hydrodynamic interactions (HI) leads to branching and string-like structures when compared to the more compact clusters that emerge without hydrodynamics.

particles become magnetized. Magnetization, in turn, results in magnetic forces between particles, see Eq. (10). Figure 1 shows snapshots for a low area fraction of $\theta \approx 0.15$ at different times, see Supplemental Movie 1 for a dynamic visualization. Both the magnetization within the particles as well as the flow field in the hydrodynamic case are visualized. Chains are formed in either case. However, chain formation is promoted by hydrodynamic coupling. Large-scale flows emerge that facilitate movement. For example, in Fig. 1(g) a chain of six particles is transported as one unit to connect with another chain into a larger structure. Without hydrodynamics, particles tend to move individually. Then, formation of larger chain-like structures is slower overall, as inferred from the upper and lower rows in Fig. 1.

The snapshots also show the strong mutual reinforcement of local magnetization for particles close to each other and oriented parallel to the external magnetic field, see Fig. 1(e). This collective effect additionally accelerates the aggregation of chains. It demonstrates the importance of spatially resolving the magnetization field, beyond the dipole assumption, specifically below magnetization saturation.

Similar effects can be observed for larger area fractions of particles. Figure 2 shows snapshots for an area fraction of $\theta \approx 0.31$, again comparing the “dry” case with the situation under hydrodynamic coupling, see also Supplemental Movie 2. In the beginning, the absence of hydrodynamics leads to faster aggregation, compare Fig. 2(b) and (f). However, chain formation is accelerated under hydro-

dynamic interactions once large-scale flows have formed. In Fig. 2(f), vortex flows occupy larger parts of the system, as magnified in Fig. 2(e).

Figure 2(d) and (h) show the developed structures after a longer time. Comparing the two cases, we observe a crucial difference. With hydrodynamic couplings, branching, string-like structures have formed. Chains of particles are on average aligned along the external magnetic field. In the absence of hydrodynamic effects, the emerging aggregates are much more compact. They consist of multiple layers of hexagonally arranged particles. This is in line with previous observations of particle aggregation under attractive isotropic interactions [34–36].

To further examine the structure formation, we introduce a chain-likeness parameter χ . It quantifies the relative number of particles in a two-neighbor configuration, that is, in a chain, compared to more compact clusters where particles have a higher number of neighbors. We define χ via

$$\chi = \frac{N_2 - (N_3 + N_4 + N_5 + N_6)}{N}. \quad (13)$$

N_j is the number of particles with j neighbors in the system. A configuration of perfect, non-branching chains leads to $\chi = 1$, whereas completely separated particles lead to $\chi = 0$. Negative values indicate that more compact clusters have formed, where particles have on average more than two neighbors. Figure 3 shows the evolution of χ for three different area fractions of particles. In each case, we repeated the calculations starting from

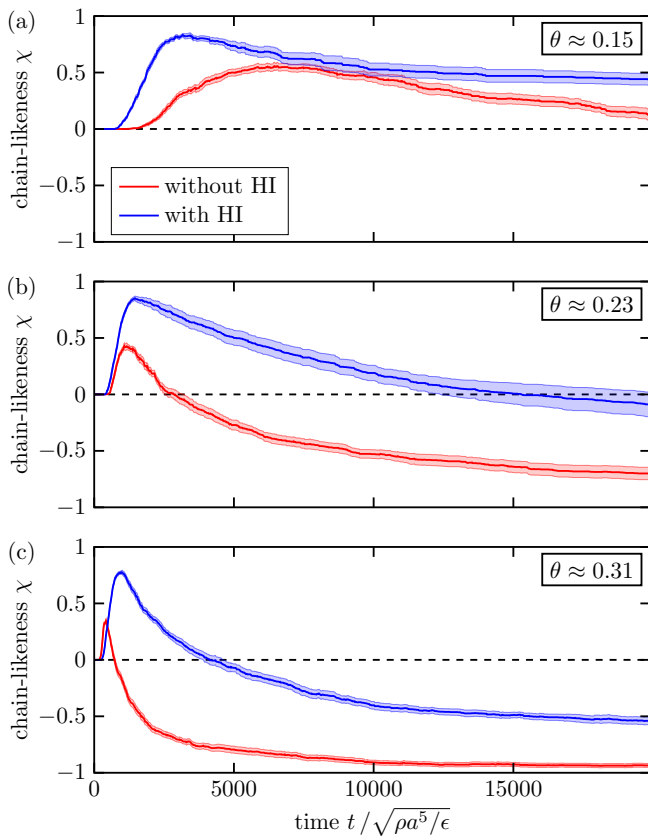


FIG. 3. Evolution of the chain-likeness parameter χ for an area fraction of (a) $\theta \approx 0.15$, (b) $\theta \approx 0.23$, and (c) $\theta \approx 0.31$. Hydrodynamic interactions (HI) consistently lead to more chain-like structures when compared to the “dry” case without HI. Shaded areas indicate standard errors, that is, standard deviations divided by the square root of the sample size.

12 different initial configurations and averaged over the results.

We first consider the small area fraction $\theta \approx 0.15$. Although slower in the absence of hydrodynamic couplings, both cases, “wet” and “dry”, exhibit the formation of chain-like aggregates in the beginning, indicated by increasing χ . After some time, χ decreases as a result of some of the chains combining into multiple-layer structures. Throughout, both the maximum and the average chain-likeness is significantly higher in the “wet” case under hydrodynamic coupling.

Increasing the area fraction to $\theta \approx 0.23$, we still observe an initial stage of chain formation. However, the subsequent decrease of χ is both faster and stronger. In the “dry” case, χ quickly dips below zero, indicating the predominance of more compact clusters. Conversely, hydrodynamic couplings lead to much slower decrease of χ . Yet, finally, negative values likewise result.

Elevated area fractions of $\theta \approx 0.31$ further amplify these effects. χ decreases very quickly to negative values

when hydrodynamic interactions are absent. It saturates close to $\chi = -1$, reflecting the formation of larger clusters, see Fig. 2(d). Turning to the case with hydrodynamics included, we observe a similar process, although much slower. The saturation value of χ seems to be higher, in line with branched, but still string-like structures as in Fig. 2(h).

Overall, the maximum of χ is consistently larger when hydrodynamic effects are included, due to the formation of single-layer, string-like chains in contrast to more compact clustering. The process of chain formation seems to be more consistent as well. In particular, the maximum of χ is always about the same height and reached after more comparable times. Conversely, the area fraction has a significantly higher impact on the dynamics in the “dry” system. Here, the initial chain formation is much faster at high area fraction compared to the slow aggregation at low area fraction. This more pronounced difference is in line with the absence of large-scale flows, which promote particle aggregation even for larger initial distances between particles under hydrodynamic coupling.

In brief, we extended the fluid particle dynamics method [34, 36] to investigate magnetically induced structure formation in magnetorheological fluids. Spatially resolved and mutual particle magnetization together with resulting elevated magnetic forces between particles are included. These effects are important below saturation magnetization. Specifically, we compare magnetically driven structure formation with and without hydrodynamic couplings. We find qualitative differences. Hydrodynamics promotes the formation of slender oriented chains and string-like structures, opposed to the more compact clusters emerging in its absence. In this way, hydrodynamic interactions serve to enhance structure formation in magnetorheological composite systems.

Besides providing a fundamental understanding of the background of structure formation in magnetic fluids in general, our results have practical implications when fabricating structured magnetorheological elastomers of improved properties. They are generated by crosslinking suspensions of magnetic particles in the presence of external magnetic fields to lock in chain-like particle aggregates [3, 5, 31]. The maximum in the chain-likeness parameter during structure formation implies an optimal time for crosslinking that leads to most pronounced chain-like structures.

The authors thank Karl Kalina for stimulating discussions and the Deutsche Forschungsgemeinschaft (German Research Foundation, DFG) for support through Research Unit FOR 5599 on structured magnetic elastomers, project no. 511114185, DFG reference nos. ME 3571/10-1 and 3571/11-1.

-
- * henning.reinken@ovgu.de
† a.menzel@ovgu.de
- [1] R. E. Rosensweig, *Ferrohydrodynamics* (Dover, Mineola, 2013).
- [2] G. Bossis, S. Lacis, A. Meunier, and O. Volkova, *J. Magn. Magn. Mater.* **252**, 224 (2002).
- [3] J. De Vicente, D. J. Klingenberg, and R. Hidalgo-Alvarez, *Soft Matter* **7**, 3701 (2011).
- [4] M. Shliomis, *Sov. Phys. JETP* **34**, 1291 (1972).
- [5] J. D. Carlson and M. R. Jolly, *Mechatronics* **10**, 555 (2000).
- [6] G. Filipcsei, I. Csetneki, A. Szilágyi, and M. Zrínyi, *Adv. Polym. Sci.* **206**, 137 (2007).
- [7] S. Behrens, *Nanoscale* **3**, 877 (2011).
- [8] S. Odenbach, *Arch. Appl. Mech.* **86**, 269 (2016).
- [9] A. K. Bastola, M. Paudel, L. Li, and W. Li, *Smart Mater. Struct.* **29**, 123002 (2020).
- [10] M. R. Jolly, J. D. Carlson, and B. C. Munoz, *Smart Mater. Struct.* **5**, 607 (1996).
- [11] X. Gong, X. Zhang, and P. Zhang, *Polym. Test.* **24**, 669 (2005).
- [12] M. Lokander and B. Stenberg, *Polym. Test.* **22**, 677 (2003).
- [13] G. Pessot, M. Schümann, T. Gundermann, S. Odenbach, H. Löwen, and A. M. Menzel, *J. Phys.: Condens. Matter* **30**, 125101 (2018).
- [14] O. V. Stolbov, Y. L. Raikher, and M. Balasoiu, *Soft Matter* **7**, 8484 (2011).
- [15] P. Metsch, K. A. Kalina, C. Spieler, and M. Kästner, *Comp. Mater. Sci.* **124**, 364 (2016).
- [16] D. Romeis, P. Metsch, M. Kästner, and M. Saphiannikova, *Phys. Rev. E* **95**, 042501 (2017).
- [17] L. Fischer and A. M. Menzel, *J. Chem. Phys.* **151**, 114906 (2019).
- [18] J. Silva, C. Gouveia, G. Dinis, A. Pinto, and A. Pereira, *Compos. Part B Eng.* **243**, 110125 (2022).
- [19] M. Roghani, D. Romeis, G. Glavan, I. A. Belyaeva, M. Shamonin, and M. Saphiannikova, *Phys. Rev. Appl.* **23**, 034041 (2025).
- [20] H. Böse, R. Rabindranath, and J. Ehrlich, *J. Intell. Mater. Syst. Struct.* **23**, 989 (2012).
- [21] R. Fuhrer, C. M. Schumacher, M. Zeltner, and W. J. Stark, *Adv. Func. Mater.* **23**, 3845 (2013).
- [22] Y. Kim and X. Zhao, *Chem. Rev.* **122**, 5317 (2022).
- [23] J. E. Martin, R. A. Anderson, D. Read, and G. Gulley, *Phys. Rev. E* **74**, 051507 (2006).
- [24] D. Ivaneyko, V. Toshchevikov, M. Saphiannikova, and G. Heinrich, *Condens. Matter Phys.* **15**, 33601 (2012).
- [25] G. Stepanov, S. Abramchuk, D. Grishin, L. Nikitin, E. Y. Kramarenko, and A. Khokhlov, *Polymer* **48**, 488 (2007).
- [26] H. Böse and R. Röder, *J. Phys.: Conf. Ser.* **149**, 012090 (2009).
- [27] Y. Han, W. Hong, and L. E. Faidley, *Int. J. Solids Struct.* **50**, 2281 (2013).
- [28] P. Cremer, H. Löwen, and A. M. Menzel, *Appl. Phys. Lett.* **107** (2015).
- [29] M. Schümann and S. Odenbach, *J. Magn. Magn. Mater.* **441**, 88 (2017).
- [30] P. Cremer, H. Löwen, and A. M. Menzel, *Phys. Chem. Chem. Phys.* **18**, 26670 (2016).
- [31] D. Günther, D. Y. Borin, S. Günther, and S. Odenbach, *Smart Mater. Struct.* **21**, 015005 (2012).
- [32] D. Faivre and D. Schuler, *Chem. Rev.* **108**, 4875 (2008).
- [33] E. Pyanzina, S. Kantorovich, J. J. Cerdà, and C. Holm, *J. Magn. Magn. Mater.* **323**, 1263 (2011).
- [34] H. Tanaka and T. Araki, *Phys. Rev. Lett.* **85**, 1338 (2000).
- [35] A. Furukawa and H. Tanaka, *Phys. Rev. Lett.* **104**, 245702 (2010).
- [36] H. Tanaka and T. Araki, *Chem. Eng. Sci.* **61**, 2108 (2006).
- [37] J. K. Dhont, *An Introduction to Dynamics of Colloids*, Vol. 2 (Elsevier, Amsterdam, 1996).
- [38] T. Richter, *Fluid-Structure Interactions: Models, Analysis and Finite Elements* (Springer, Cham, 2017).
- [39] H. Kodama, K. Takeshita, T. Araki, and H. Tanaka, *J. Phys.: Condens. Matter* **16**, L115 (2004).
- [40] A. Furukawa, D. Marenduzzo, and M. E. Cates, *Phys. Rev. E* **90**, 022303 (2014).
- [41] A. M. Menzel, T. Ohta, and H. Löwen, *Phys. Rev. E* **89**, 022301 (2014).
- [42] M. Tateno and H. Tanaka, *Nature Commun.* **12**, 912 (2021).
- [43] A. Furukawa, M. Tateno, and H. Tanaka, *Soft Matter* **14**, 3738 (2018).
- [44] I. Steinbach, *Model. Simul. Mater. Sci. Eng.* **17**, 073001 (2009).
- [45] R. Qin and H. Bhadeshia, *Mater. Sci. Technol.* **26**, 803 (2010).
- [46] M. Puljiz, S. Huang, K. A. Kalina, J. Nowak, S. Odenbach, M. Kästner, G. K. Auernhammer, and A. M. Menzel, *Soft Matter* **14**, 6809 (2018).
- [47] S. R. De Groot and L. G. Suttrop, *Foundations of Electrodynamics* (North-Holland, Amsterdam, 1972).
- [48] A. C. Eringen and G. A. Maugin, *Electrodynamics of Continua I: Foundations and Solid Media* (Springer, New York, 1990).
- [49] P. Metsch, K. Kalina, J. Brummund, and M. Kästner, *Arch. Appl. Mech.* **89**, 47 (2019).
- [50] C. Canuto, M. Y. Hussaini, A. Quarteroni, and T. A. Zang, *Spectral Methods: Evolution to Complex Geometries and Applications to Fluid Dynamics* (Springer, Berlin Heidelberg, 2007).
- [51] See the Supplemental Material for more details on rescaling the equations and the numerical implementation, as well as more information on the Supplemental Movies.

Hydrodynamics substantially affects induced structure formation in magnetic fluids

Supplemental Material

Henning Reinken,^{1,*} Markus Heiber,¹ Takeaki Araki,² and Andreas M. Menzel^{1,†}

¹*Institut für Physik, Otto-von-Guericke-Universität Magdeburg, Universitätsplatz 2, 39106 Magdeburg, Germany*

²*Department of Physics, Kyoto University, Kyoto 606-8502, Japan*

(Dated: February 5, 2026)

This Supplemental Material discusses how the equations introduced in the main text are rescaled for the purposes of numerical calculations, gives more details on the numerical methods and includes additional information on the Supplemental Movies.

I. RESCALING

We rescale the equations to reduce the number of free parameters. To this end, we employ the particle radius a as spatial scale and utilize the strength ϵ of the Lennard–Jones potential to define a time scale. Thus, we rescale space and time via

$$x = a\tilde{x}, \quad t = \sqrt{\frac{a^5\rho}{\epsilon}}\tilde{t}, \quad (\text{S1})$$

where the tilde indicates rescaled units. The rescaled Navier–Stokes equation is then obtained as

$$\partial_{\tilde{t}}\tilde{\mathbf{v}} + \tilde{\mathbf{v}} \cdot \tilde{\nabla}\tilde{\mathbf{v}} = \tilde{\mathbf{f}} - \tilde{\nabla}\tilde{p} + C_{\text{visc}}\tilde{\nabla} \cdot [\tilde{\eta}\{(\tilde{\nabla}\tilde{\mathbf{v}}) + (\tilde{\nabla}\tilde{\mathbf{v}})^{\top}\}], \quad (\text{S2})$$

with $\tilde{\eta}(\tilde{\mathbf{r}}) = 1 + \sum_{i=1}^N (R-1)\phi_i(\tilde{\mathbf{r}})$ and $\tilde{p} = a^3 p/\epsilon$. The strength of viscous forces compared to the inter-particle potential is characterized by $C_{\text{visc}} = \eta_s \sqrt{a}/(\rho\epsilon)$. Throughout the work, we set $C_{\text{visc}} = 1$. We determine particle-based Reynolds numbers Re_i , employing the particle diameter $2a$, the viscosity η_s of the surrounding fluid and the current particle velocity \mathbf{V}_i via $\text{Re}_i = 2a\rho|\mathbf{V}_i|/\eta_s$. Maximum observed Reynolds numbers are of the order of $\text{Re}_i \approx 10^{-2}$. Thus, for the chosen value of C_{visc} , viscous effects dominate over inertia.

The magnetization \mathbf{M} , magnetic flux density \mathbf{B} , and magnetic field \mathbf{H} are rescaled using the saturation magnetization M_{sat} and vacuum magnetic permeability μ_0 ,

$$\mathbf{M} = M_{\text{sat}}\tilde{\mathbf{M}}, \quad \mathbf{H} = M_{\text{sat}}\tilde{\mathbf{H}}, \quad \mathbf{B} = \mu_0 M_{\text{sat}}\tilde{\mathbf{B}}. \quad (\text{S3})$$

Consequently, the rescaled equation for the magnetization reads

$$\tilde{\mathbf{M}} = \left[\coth(\tilde{\alpha}\phi_{\text{tot}}|\tilde{\mathbf{H}}|) - \frac{1}{\tilde{\alpha}\phi_{\text{tot}}|\tilde{\mathbf{H}}|} \right] \frac{\tilde{\mathbf{H}}}{|\tilde{\mathbf{H}}|}, \quad (\text{S4})$$

where $\tilde{\alpha} = \alpha M_{\text{sat}}$. Throughout our work, we use $\tilde{\alpha} = 39.3$. This corresponds to $M_{\text{sat}} = 3.333 \times 10^5 \text{ A m}^{-1}$ and $\alpha = 1.179 \times 10^{-4} \text{ m A}^{-1}$, which is appropriate for nickel

particles [1]. Magnetic forces entering the force density $\tilde{\mathbf{f}}$ in the Navier–Stokes equation are calculated in rescaled units via

$$\tilde{\mathbf{F}}_i^{\text{mag}} = C_{\text{mag}} \int d\tilde{\mathbf{r}} \tilde{\mathbf{M}}_i \cdot \tilde{\nabla}\tilde{\mathbf{B}}. \quad (\text{S5})$$

Their overall strength compared to the inter-particle potential is characterized by $C_{\text{mag}} = \mu_0 M_{\text{sat}}^2 a^3/\epsilon$. We set $C_{\text{mag}} = 1$ throughout.

II. NUMERICAL METHODS

The simulation method of fluid particle dynamics [2] involves a combination of a discrete particle picture and a hydrodynamic field description. Connections between these two levels of description are based on phase-fields ϕ_i to represent the presence of each particle i . They vary smoothly from the inside to the outside of the particles.

All fields are evaluated numerically, using grids with different resolution for the hydrodynamic quantities such as the velocity field \mathbf{v} and the magnetic quantities such as the magnetization \mathbf{M} and the magnetic field \mathbf{H} . This approach allows for a very efficient implementation. To obtain the results discussed in this work, we use a spatial resolution of 320×320 grid points for the hydrodynamic calculations. The interface thickness of the transition region, see Eq. (1) in the main text, is set to $c = 0.2a$ for the hydrodynamic calculations. For the magnetic quantities, we use a resolution of 640×640 grid points and $c = 0.1a$. The factor R , which characterizes how strongly the viscosity is increased within the particles, see Eq. (3) in the main text, is set to $R = 50$. This value was shown to be sufficient in previous studies [2].

We utilize a pseudospectral method [3], that is, spatial derivatives are calculated in Fourier space, which benefits from the efficient implementation of the Fast Fourier Transform. Throughout this work, we consider periodic boundary conditions. We fix the system size to $32a \times 32a$ and vary the number of particles. Specifically, we choose 50, 75, and 100 particles, which yields area fractions of $\theta \approx 0.15$, $\theta \approx 0.23$, and $\theta \approx 0.31$.

As summarized in the main text, the basic procedure in every time step involves, first, the calculation of magnetic and other forces between particles. Second, these

* henning.reinken@ovgu.de

† a.menzel@ovgu.de

enter the hydrodynamic description as a force density. Third, the resulting velocity field then leads to particle motion, producing an updated particle configuration. In the following, we outline these steps in more detail.

In every time step, we obtain the magnetization field \mathbf{M} , magnetic flux density \mathbf{B} , and magnetic field \mathbf{H} by simultaneously solving Eq. (S4) and the Maxwell equations, see Eqs. (8) in the main text. Here, we distinguish between the uniform external magnetic field \mathbf{H}_{ext} and the additional inhomogeneous internal magnetic field \mathbf{H}_{inh} induced by the magnetization of the particles themselves. The total magnetic field is given as the sum of both terms, $\mathbf{H} = \mathbf{H}_{\text{ext}} + \mathbf{H}_{\text{inh}}$. To solve Maxwell's equations, we further introduce a scalar potential ψ for the inhomogeneous part of the magnetic field, $\mathbf{H}_{\text{inh}} = -\nabla\psi$. As a result, \mathbf{H} always satisfies Ampère's law, $\nabla \times \mathbf{H} = \mathbf{0}$. Substituting $\mathbf{B} = \mu_0(\mathbf{M} + \mathbf{H})$ into Gauss's law, $\nabla \cdot \mathbf{B} = 0$, we obtain

$$\nabla^2\psi = \nabla \cdot \mathbf{M}, \quad (\text{S6})$$

which is solved in Fourier space.

These equations are combined in an iterative procedure that involves the following steps. We first obtain an initial iteration of the magnetization field via Eq. (S4) based on the magnetic field \mathbf{H} of the last step. Then, we calculate the corresponding scalar potential ψ via Eq. (S6) from the magnetization field \mathbf{M} . It provides an updated magnetic field, which we then use to correct the magnetization field, starting the next step of iteration. To guarantee stability, we further introduce an under-relaxation procedure in the calculation of \mathbf{M} . As a termination condition, we track the relative local change in the magnetization field and consider the solution to be converged once the maximum local change per iteration step is below 0.1%. For the calculation of the magnetic forces via Eq. (S5), we need the magnetic flux density, which is readily obtained from the magnetization \mathbf{M} and magnetic field \mathbf{H} via $\mathbf{B} = \mu_0(\mathbf{M} + \mathbf{H})$.

All inter-particle magnetic forces as well as the Lennard–Jones forces are combined into a single force density for the current particle configuration via Eq. (5) in the main text. It then enters the hydrodynamic calculations. The Navier–Stokes equation is discretized in time via the implicit Euler method. For every time step, this yields an implicit equation for the velocity field in the new time step, which we solve iteratively in Fourier space via an under-relaxation procedure. Analogously to the iteration procedure in the context of the magnetic quantities, we track the relative local change in the velocity field and consider the solution to be converged once

the maximum local change per iteration step is below 0.1%. Simultaneously, the pressure is determined such that the velocity field stays divergence-free and the incompressibility condition is fulfilled [3].

Finally, having obtained the velocity field, we go back to the discrete particle level by calculating the discrete particle velocities \mathbf{V}_i for every particle i via Eq. (11) in the main text. Then, the particle positions are updated by an explicit Euler step as

$$\mathbf{R}_i(t + \Delta t) = \mathbf{R}_i(t) + \Delta t \mathbf{V}_i(t). \quad (\text{S7})$$

Using the new particle configuration, the fields ϕ_i are then updated as well, which completes the time step.

In the case without explicit hydrodynamic interactions, the many-particle system is governed by underdamped dynamics, including a linear friction term, see Eq. (12) in the main text. Here, we calculate the particle velocities and updated positions directly from the current forces via an explicit Euler procedure,

$$\begin{aligned} \mathbf{V}_i(t + \Delta t) &= \mathbf{V}_i(t) + \Delta t [\mathbf{F}_i(t) - \gamma \mathbf{V}_i(t)], \\ \mathbf{R}_i(t + \Delta t) &= \mathbf{R}_i(t) + \Delta t \mathbf{V}_i(t). \end{aligned} \quad (\text{S8})$$

For the case with full hydrodynamic interactions, the time step is set to $\Delta t = 2$, whereas for the dynamics without hydrodynamic interactions, we have to use a much smaller step $\Delta t = 0.01$ due to the explicit Euler method. To speed up the calculations, the magnetization field and magnetic forces are only recalculated every 100 time steps in the case without hydrodynamics, which is still double the frequency compared to the case with full hydrodynamics.

III. INFORMATION ON THE SUPPLEMENTAL MOVIES

The Supplemental Movies provide dynamic visualizations of the structure formation of magnetizable particles subject to an external magnetic field. We compare the cases including and excluding hydrodynamic coupling for area fractions $\theta \approx 0.15$ (Supplemental Movie 1) and $\theta \approx 0.31$ (Supplemental Movie 2). In both movies, the “dry” case without hydrodynamics is depicted on the left, whereas the impact of full hydrodynamic coupling is shown on the right. As in the snapshots in Fig. 1 and 2 in the manuscript, the color scale refers to the magnetization field and the blue arrows indicate emerging flow fields of the carrier liquid. The duration of both movies covers 20000 time units.

[1] M. Puljiz, S. Huang, K. A. Kalina, J. Nowak, S. Odenbach, M. Kästner, G. K. Auernhammer, and A. M. Menzel, *Soft Matter* **14**, 6809 (2018).
 [2] H. Tanaka and T. Araki, *Phys. Rev. Lett.* **85**, 1338 (2000).

[3] C. Canuto, M. Y. Hussaini, A. Quarteroni, and T. A. Zang, *Spectral Methods: Evolution to Complex Geometries and Applications to Fluid Dynamics* (Springer, Berlin Heidelberg, 2007).